



The effect of grain boundary character distribution on the mechanical properties at different strain rates of a 316L stainless steel

Zhen Zhuo¹, Shuang Xia^{1,2}, Qin Bai^{1,3,*}, and Bangxin Zhou^{1,2}

¹School of Materials Science and Engineering, Shanghai University, Shanghai 200072, People's Republic of China

²State Key Laboratory of Advanced Special Steel, Shanghai University, Shanghai 200072, People's Republic of China

³Key Laboratory for Microstructures, Shanghai University, P.O. Box 129, 99 Shangda Road, Shanghai 200444, People's Republic of China

Received: 26 June 2017

Accepted: 9 October 2017

Published online:
16 October 2017

© Springer Science+Business
Media, LLC 2017

ABSTRACT

Grain boundary engineering was applied to a 316L stainless steel. The proportion of low- Σ coincidence site lattice boundaries was increased to more than 70% in the GBE specimen. The effect of grain boundary character distribution formed through GBE on the mechanical properties at different strain rates (4×10^{-2} , 4×10^{-3} , 4×10^{-4} , 4×10^{-5} s⁻¹) was studied by tensile test at room temperature. The results showed that the GBE specimens exhibited higher uniform elongation than the non-GBE specimens. With the strain rate decreasing, the uniform elongations of GBE specimens had a greater extent of increase. The local misorientation, average Schmid factor (\bar{m}) and Taylor factor (M) in GBE and non-GBE specimens at uniform plastic deformation area were studied by using electron backscatter diffraction. The results indicate that the micro-zone strain was more uniformly distributed and the activation process of the slip system was apt to happen in the GBE specimens.

Introduction

Stainless steels exhibit a combination of good corrosion resistance and mechanical properties and thus have been widely used in many fields, such as petrochemical industry and nuclear industry. In response to a steady increase in demand, stainless steel production has an average annual growth rate of 5% over the last 10 years [1]. With prolonged service life and improved performance being demanded

by industry, the need to further improve the performance of stainless steels should be considered. In polycrystalline materials, the grain boundaries (GBs) are extremely important and greatly influence properties of the materials. For instance, the transmission of dislocations across GBs is an important step in controlling the deformation behavior of the materials [2]. In addition, GB segregation [3–5], creep resistance [6, 7] and corrosion resistance [8–11] are also affected by the GB structure. Therefore, the characters of GBs

Address correspondence to E-mail: baiqin31@shu.edu.cn; xs@shu.edu.cn

[12] play a very important role in grain-boundary-related properties and various properties can be improved by changing grain boundary character distribution (GBCD).

Since Watanabe [13] proposed the concept of “grain boundary design and control” in 1984, the research field of grain boundary engineering (GBE) has developed a lot. The proportion of low- Σ CSL ($\Sigma \leq 29$, coincidence site lattice) grain boundaries in the materials with face-centered cubic (FCC) structure and low stacking fault energy (SFE) can be significantly enhanced by appropriate thermomechanical processing (TMP) [14–17]. The low- Σ CSL GBs differ in properties from random high-angle GBs in terms of their structure and energy [18]. The important aspects of the GBE are the proportion of low- Σ CSL GBs and the GB network they formed [19].

GBE has been successfully applied to many structural materials, such as austenitic stainless steels [20, 21], Ni-based alloys [22] and copper alloys [23]. In recent years, some work has been carried out to study the effects of GBCD on the mechanical properties of various austenitic stainless steels. Kobayashi et al. [24] investigated the fatigue crack propagation in austenitic stainless steels and found that the propagation rate of fatigue crack was lower for the specimen with a higher fraction of low- Σ CSL GBs (73%) including $\Sigma 3$ GBs (58%) than for the specimen with a lower fraction of low- Σ CSL GBs (53%) including $\Sigma 3$ GBs (39%). According to the results given by Kumar et al. [2], the enhanced proportion of special GBs would decrease the yield strength and increase the percent elongation of 304L stainless steel. The results of Sinha [25] showed that the copper containing austenitic stainless steel sample with a high frequency of low- Σ CSL GBs produced by GBE processing exhibited higher ductility than the conventionally processed sample. However, the grain sizes of these samples after TMPs are different. In these papers, the GBCDs of the materials were studied with respect to the applied GBE processing and consequent improvements in mechanical properties were reported. Grain size is a key factor to

affect mechanical properties of materials following the well-known Hall–Petch relationship [26]. Schino et al. [27] showed that the micro-hardness of austenitic steel increases with decreasing grain size, as does the yield and flow stress. In addition, Wang et al. [28] studied the effect of GBs on cyclic deformation behavior and showed that large-angle random GBs obstructing the passage of persistent slip bands (PSBs) were common phenomena and thus showed a strong effect on fatigue damage. In another study, Detrois et al. [29] found that the strain rate also influences on stress–strain behavior by changing GBCD of Ni-based superalloy RR1000. The fraction of $\Sigma 3$ GBs remained nominally unchanged following compression at the strain rate of 0.001 s^{-1} . While as the compression strain rates increased to 0.05 s^{-1} , a larger decrease in the fraction of $\Sigma 3$ boundaries was measured down to 6%. The maximum stress also increased from 92 MPa at 0.001 s^{-1} to 252 MPa at 0.05 s^{-1} . In this paper, different TMPs were applied to a 316L stainless steel (316LSS) to obtain GBE specimens and non-GBE specimens with similar average grain sizes. Subsequently, the effect of the microstructure after GBE processing on the mechanical properties at different strain rates was investigated.

Experimental procedure

Material and experimental method

The chemical composition of the 316LSS specimens used in this study is presented in Table 1. The starting condition of the materials was cold rolled with the thickness reduction of 50% and subsequently solution annealed at $1150 \text{ }^\circ\text{C}$ for 30 min followed by water quenching. The TMPs of GBE were carried out on some of the solution-annealed specimens with 7% tensile deformation prior to annealing at $1050 \text{ }^\circ\text{C}$ for 30 min followed by water quenching. The design of tensile specimen is shown in Fig. 1. The long axis of the specimens coincides with the rolling direction.

Table 1 Chemical composition of 316L stainless steel (in wt %)

SS	C	Si	Mn	P	S	Cr	Ni	Mo	Fe
316L	0.012	0.22	1.27	0.017	0.001	17.65	13.40	2.30	Balance

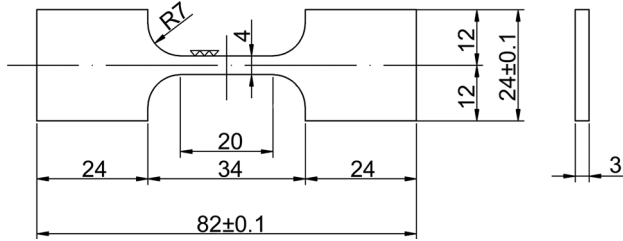


Figure 1 Geometry of tensile specimen (unit: mm).

The specimens measuring 20 mm in gauge length, 4 mm in width and 3 mm in thickness were machined using wire cut electrical discharge machine. Tensile tests were conducted at room temperature under displacement control at different strain rates (4×10^{-2} , 4×10^{-3} , 4×10^{-4} , $4 \times 10^{-5} \text{ s}^{-1}$) using the MTS CMT5305 microcomputer-controlled electron universal testing machine.

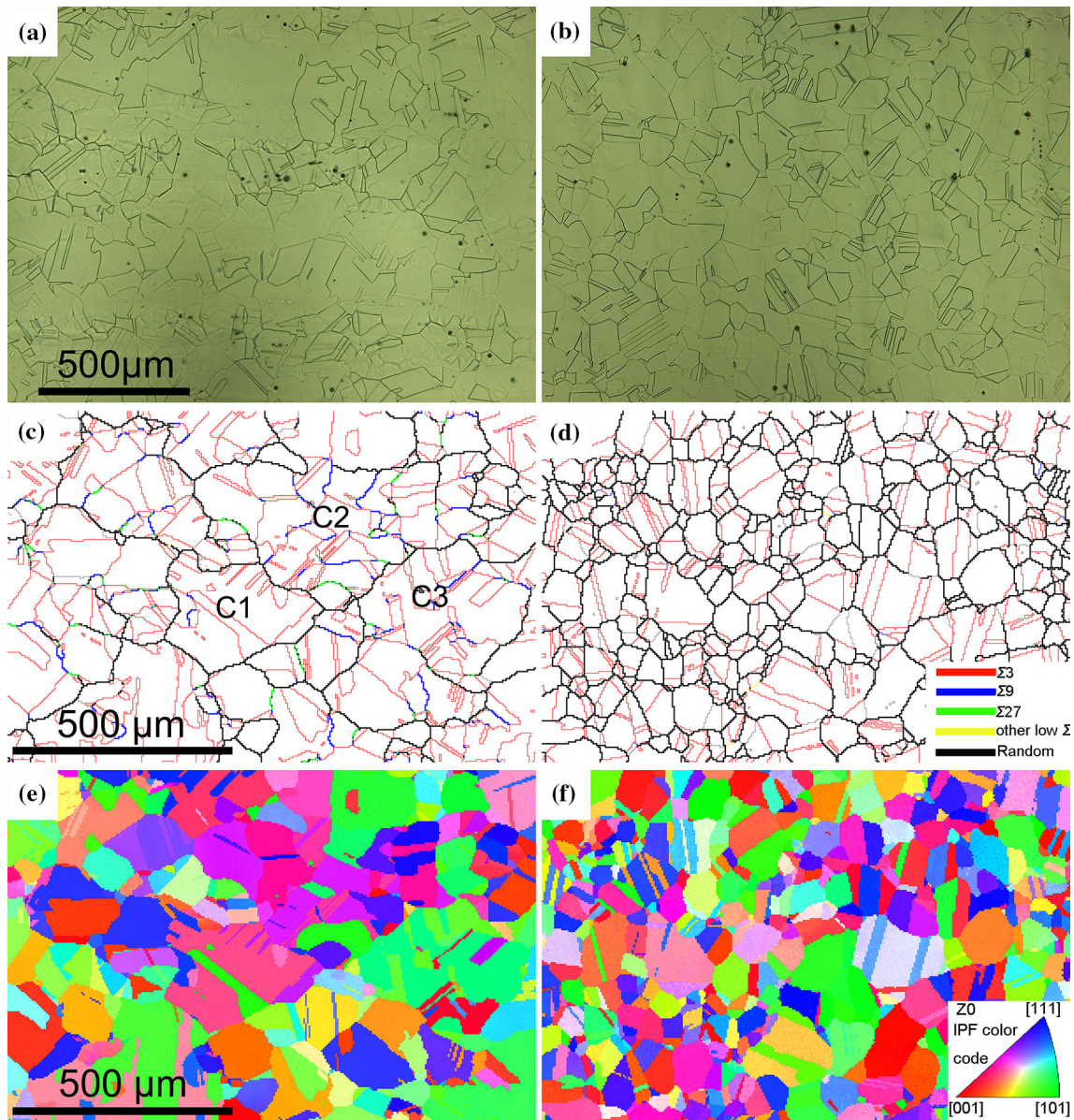


Figure 2 a, b OM images, c, d distributions of the types of grain boundaries and e, f orientation distributions of grains in a, c, e GBE specimens and b, d, f non-GBE specimens (in the GBE

specimen, the formed grain clusters C1, C2 and C3 enclosed by random boundary (R) consist of grains with $\Sigma 3^n$ orientation relationships).

Characterization methods

The specimens for electron backscatter diffraction (EBSD) experiments were sequentially grinded using SiC papers to 400, 800, 1000, 1200, 1500 and 2000 grit and subsequently electro-polished in a solution of 20% HClO₄ + 80% CH₃COOH at room temperature with 40 V direct current for 2–3 min. Metallographic specimens were etched for 20–30 min in an etching solution containing 10% HNO₃ + 3% HF + 87% H₂O and measured with KEYENCE VH-Z100 optical microscopy (OM). The crystallographic orientation was characterized with HKL Technology EBSD system attached to a CamScan Apollo 300 thermal field emission gun scanning electron microscope (SEM). The operation conditions are 20 kV accelerating voltage, 30 mm working distance and 70° beam incidence angle. The EBSD analysis was performed using a step size of 4 μm depending on grain size. An area of 1200 μm × 800 μm was scanned on each specimen. The CSL boundaries were defined according to the Palumbo–Aust criterion ($\Delta\theta_{\max} = 15^\circ \Sigma^{-5/6}$) [30]. The EBSD data were analyzed by using the HKL Channel5 and TSL OIM 7.2 softwares. The average grain size and average grain

cluster size of the tested specimens are calculated by equivalent circle diameter (ECD) in the Channel5 (Annealing twins are also regarded as grains during calculating the grain size).

Results and discussion

Microstructure and grain boundary character distribution

The microstructures and grain boundary characters obtained from EBSD analysis are given in Fig. 2. Figure 2a, b shows the optical micrographs for the GBE and non-GBE specimens, respectively. Many straight single line or parallel line pairs can be observed as shown in Fig. 2. Both of them are the annealing twins ($\Sigma 3$ boundaries). Distributions of the types of grain boundaries of the GBE and non-GBE specimens are shown in Fig. 2c, d. Different colors are used to show the different type grain boundaries. As shown in Fig. 2c, a large number of $\Sigma 3$ boundaries (red) appear in the GBE specimen which is consistent with the observation of optical microscopy. During recrystallization, annealing twins and its variants were produced through extensive multiple twinning forming a large amount of interconnected $\Sigma 3^n$ ($n = 1, 2, 3...$) type boundaries. The $\Sigma 3^n$ grain boundaries connected with each other forming many triple junctions, such as $\Sigma 3$ – $\Sigma 3$ – $\Sigma 9$, $\Sigma 3$ – $\Sigma 9$ – $\Sigma 27$, inside the area encircled by random grain boundaries (black) [20]. The grain boundary network (GBN) of GBE specimen was featured by the formation of large grain clusters produced by multiple twinning, as shown in Fig. 2c C1, C2 and C3. The orientation distributions of grains for the GBE and non-GBE specimens, respectively, as shown in Fig. 2e, f, reveal a fully recrystallized microstructure with no obvious texture. The deviation from ideal CSL misorientations is very important in affecting the properties of grain boundaries. Figure 3 shows the distribution plot of deviations of $\Sigma 3$

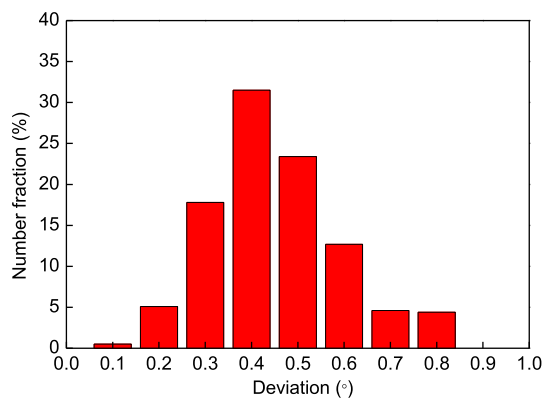


Figure 3 Deviation degrees from ideal $\Sigma 3$ misorientation of the GBE specimen.

Table 2 Grain boundary character distribution and grain sizes of the GBE and non-GBE specimens

Specimen	Length fraction of grain boundary (%)			Average grain size (μm)	Average grain cluster size (μm)
	$\Sigma 3$	$\Sigma 9 + \Sigma 27$	Overall low- Σ		
GBE	65.0	8.7	73.7	27.6	135.2
non-GBE	42.9	0.6	43.8	28.2	60.6

Annealing twins are also regarded as grains during calculating the grain size

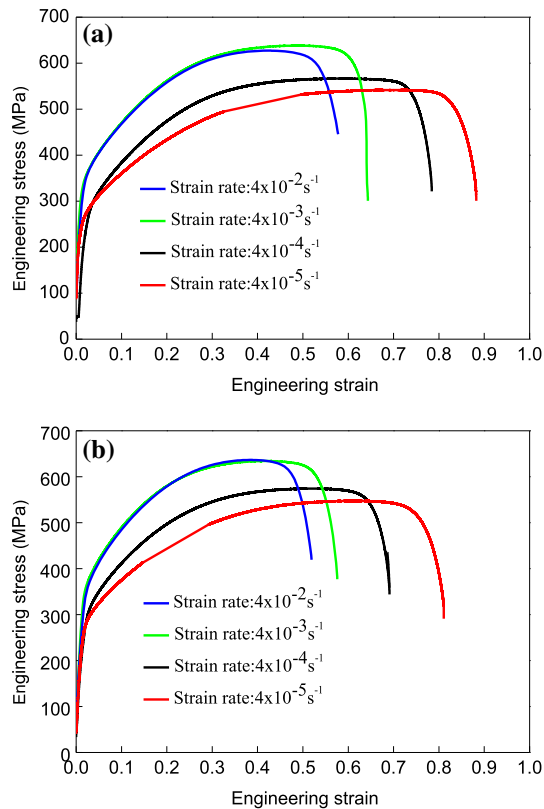


Figure 4 Tensile test curves showing the plot of engineering stress versus engineering strain for **a** GBE specimens and **b** non-GBE specimens at different strain rates.

boundaries from the ideal $60^\circ \langle 111 \rangle$ misorientation for the GBE specimen where 200 boundaries are included for the statistical analysis. The peak with a high number fraction occurring between 0.3° and 0.5° indicates that $\Sigma 3$ boundaries in this specimen have very low deviations from the ideal misorientation. Therefore, almost all of the $\Sigma 3$ boundaries are “twin” type.

Table 2 presents the low- Σ CSL grain boundary proportions, average grain sizes and average grain cluster sizes as obtained from the EBSD analysis for the GBE and non-GBE specimens. As shown in Table 2, the proportion of low- Σ CSL GBs is enhanced from 43.8 to 73.7% after GBE processing. In addition, in the GBE specimen, most of the low- Σ CSL GBs are $\Sigma 3$ twin boundaries with a length fraction of 65.0% and the sum of $\Sigma 9 + \Sigma 27$ fraction is 8.7%. Table 2 also shows that GBE and non-GBE specimens have similar average grain size: 27.6 and 28.2 μm , respectively. However, average grain cluster size of the GBE specimen is 135.2 μm and much larger than 60.6 μm of the non-GBE specimen.

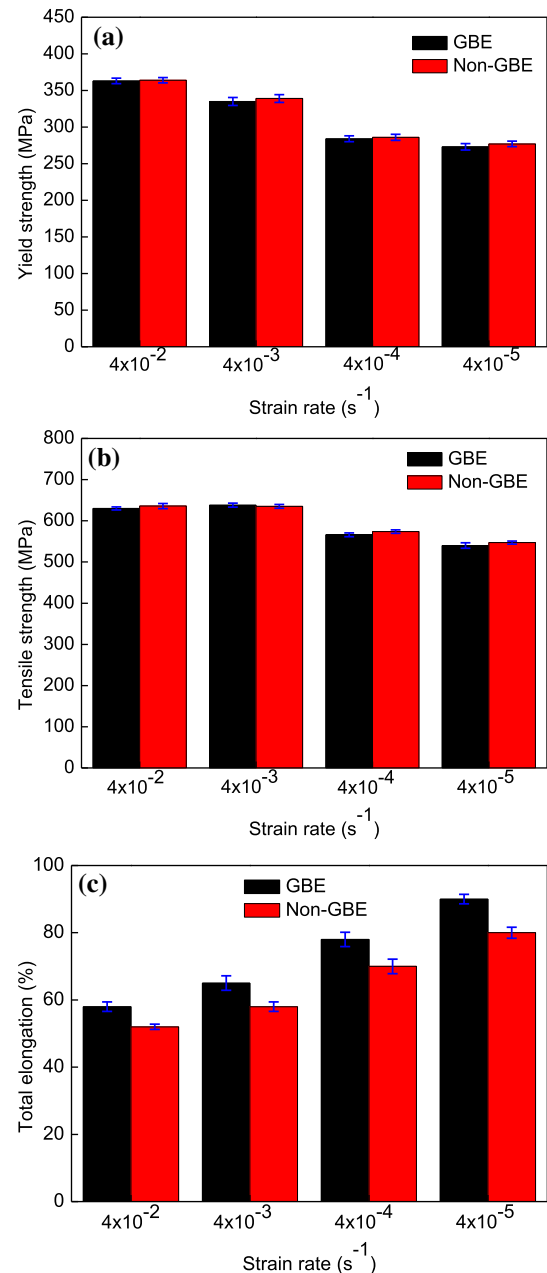


Figure 5 **a** Variation of yield strength, **b** tensile strength and **c** total elongation with strain rate for GBE specimens and non-GBE specimens.

Mechanical properties

The tensile curves showing engineering stress against engineering strain of GBE and non-GBE specimens at different strain rates are presented in Fig. 4a, b, respectively. It can be seen that the strain rate has a very significant effect on the stress–strain behavior of both specimens. Figure 5 shows the variation of yield strength, tensile strength and total elongation with

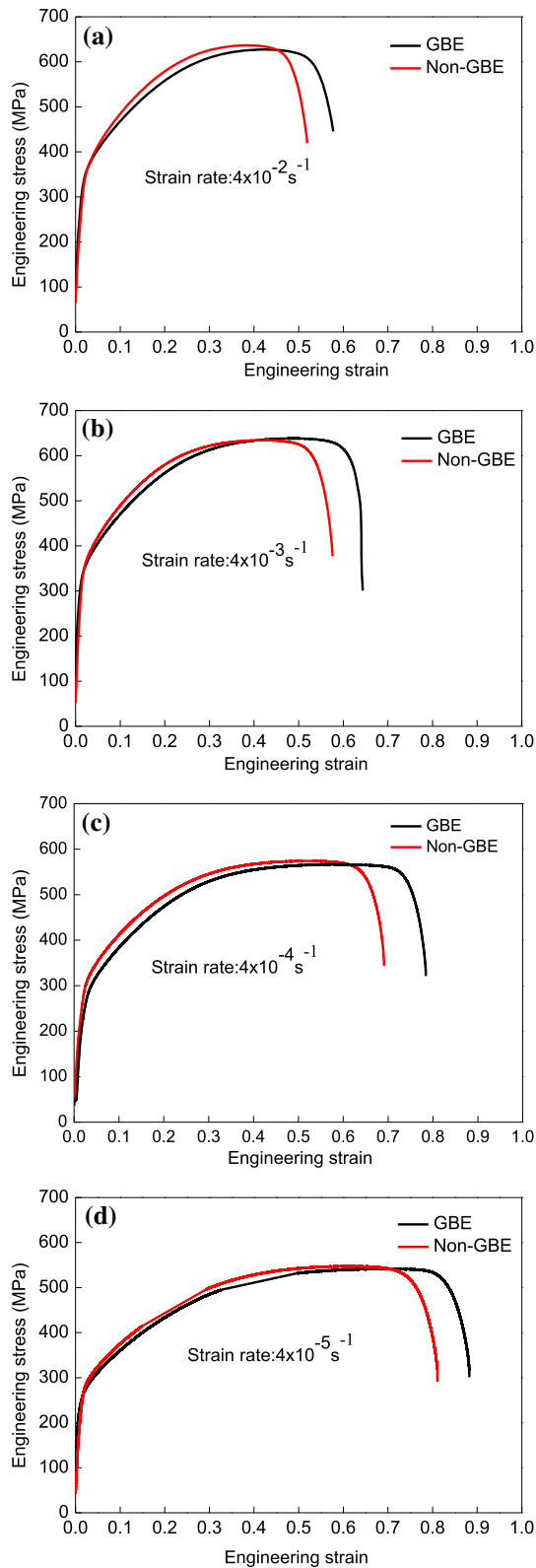


Figure 6 Comparison of engineering strain–stress curves of GBE and non-GBE specimens at the strain rates of **a** $4 \times 10^{-2} \text{ s}^{-1}$, **b** $4 \times 10^{-3} \text{ s}^{-1}$, **c** $4 \times 10^{-4} \text{ s}^{-1}$, **d** $4 \times 10^{-5} \text{ s}^{-1}$.

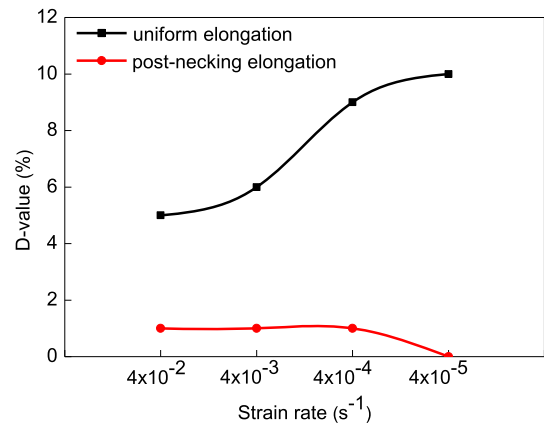


Figure 7 Variation of *D* values of uniform elongation and *D* values of post-necking elongation for GBE and non-GBE specimens with different strain rates.

strain rate for GBE specimens and non-GBE specimens. As can be seen from Fig. 5a, the yield strengths of both GBE and non-GBE specimens are observed to decrease dramatically as a function of strain rate and ranged from 365 MPa at $4 \times 10^{-2} \text{ s}^{-1}$ to about 275 MPa at $4 \times 10^{-5} \text{ s}^{-1}$. This phenomenon is attributed to the strong influence of strain rate on dislocation motion. As observed previously by Lichtenfeld et al. [31], the increase in dislocation density leading to severe work-hardening tendency was attributed to dislocation tangle at higher strain rate. So, a higher strain rate results in a higher yield strength. Figure 5b shows that these two specimens exhibit very strong dependence of tensile strength on strain rate. When the strain rate decreases from 4×10^{-2} to $4 \times 10^{-3} \text{ s}^{-1}$, the tensile strength does not change significantly (about 635 MPa). In this strain rate region, the tensile strength is not sensitive to strain rate, which correlates with the occurrence of inhomogeneous plastic deformation in most of the grains. When the strain rate continues to decrease to $4 \times 10^{-5} \text{ s}^{-1}$, the tensile strength decreases obviously from 635 MPa to about 545 MPa due to more and more uniform plastic deformation of grains showing a strong strain rate sensitivity [32]. Liu et al. [33] also studied the strain rate sensitivity and divided the region of strain rate into insensitive and sensitive regions. Additionally, as shown in Fig. 5c, the total elongations of both specimens are also observed to increase about 30% as strain rate decreases from 4×10^{-2} to $4 \times 10^{-5} \text{ s}^{-1}$. The trend is due to delayed necking at lower strain rate.

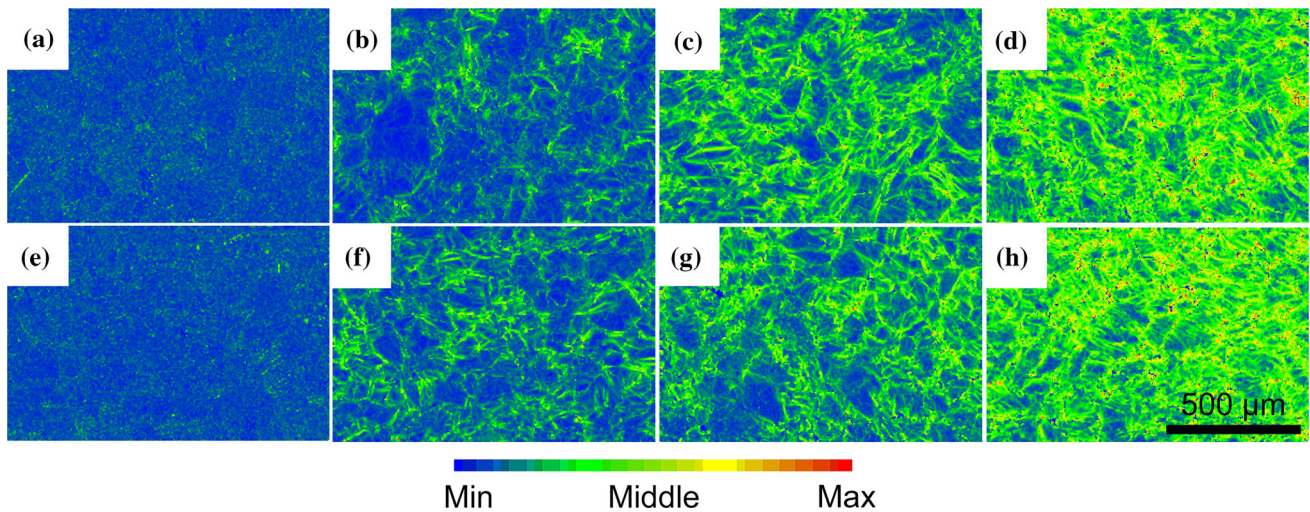


Figure 8 Local misorientation maps for GBE and non-GBE specimens after different tensile deformations. **a** GBE-0, **b** GBE-5%, **c** GBE-10%, **d** GBE-20%, **e** non-GBE-0, **f** non-GBE-5%, **g** non-GBE-10%, **h** non-GBE-20%.

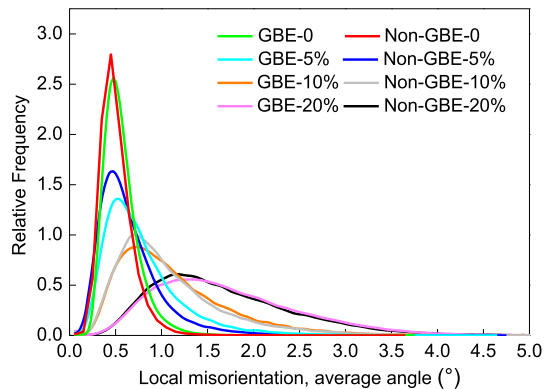


Figure 9 Local misorientation versus relative frequency for the GBE and non-GBE specimens under different deformation conditions.

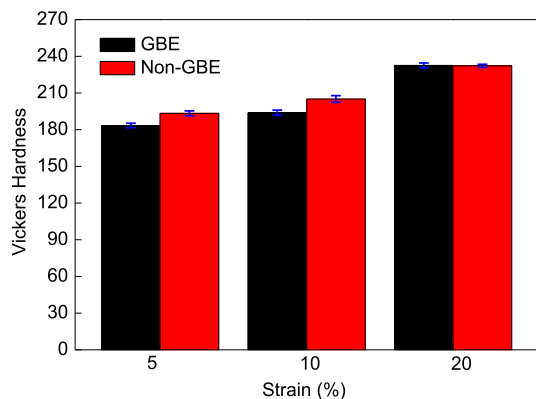


Figure 10 Vickers hardness of GBE and non-GBE specimens under different deformation conditions.

Figure 6 shows the comparison of engineering stress–strain curves at different strain rates of GBE and non-GBE specimens. As shown in Fig. 6a–d, the total elongations of GBE specimens are greater than that of non-GBE specimens at all the tested strain rates. The total elongation can be divided into two parts: uniform elongation (UE) and post-necking elongation (PE) [34]. Therefore, in order to investigate the difference of elongations between GBE and non-GBE specimens, D values of uniform elongation ($UE_{\text{GBE}} - UE_{\text{non-GBE}}$) and D values of post-necking elongation ($PE_{\text{GBE}} - PE_{\text{non-GBE}}$) in room temperature tests as a function of strain rate are shown in Fig. 7. It can be observed that the influence of GBCD on total elongation is evident with regard to the increased uniform elongation. In addition, one can see that as the strain rate decreases from 4×10^{-2} to $4 \times 10^{-5} \text{ s}^{-1}$, D values of uniform elongation increase from 5 to 10%. The result shows that low- Σ CSL GBs are much more effective for improving uniform plastic deformation of the GBE specimen under the condition of low strain rate, while the D values of post-necking elongation keep almost constant with strain rate.

Local misorientation and Schmid factor

The examinations of local misorientation and Schmid factor distribution for the GBE and non-GBE specimens in the uniform plastically deforming area were made in order to study the effect of GBCD on uniform elongation. The deformed specimens at the

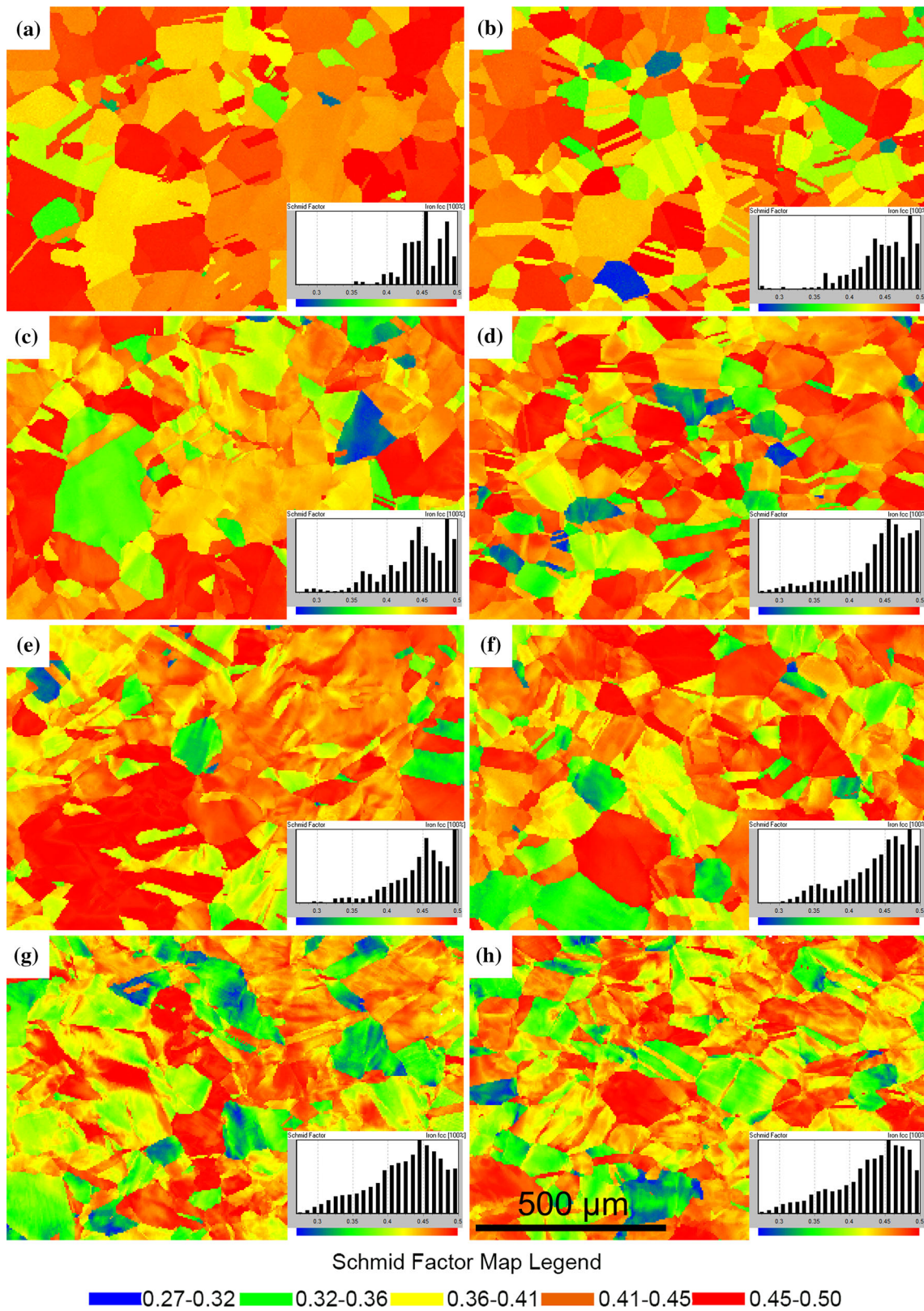


Figure 11 Schmid factor maps for GBE and non-GBE specimens after different tensile deformations. **a** GBE-0, **b** non-GBE-0, **c** GBE-5%, **d** non-GBE-5%, **e** GBE-10%, **f** non-GBE-10%, **g** GBE-20%, **h** non-GBE-20%.

strain rate of $4 \times 10^{-4} \text{ s}^{-1}$ are designated as GBE-5%, non-GBE-5%, GBE-10%, non-GBE-10%, GBE-20% and non-GBE-20% for the microstructure examinations. GBE-5% stands for GBE specimens with tensile deformation of 5%; non-GBE-5% stands for non-GBE specimens with tensile deformation of 5% and so on.

Figure 8 shows the local misorientation maps for GBE and non-GBE specimens after different tensile deformations. Local misorientation is calculated by taking the average misorientation between each measurement point and its eight neighbors excluding grain boundaries, and it highlights local strain variations independent of grain size [35]. As shown in Fig. 8, it is obvious that with the increase in deformation, the local misorientation in the specimens increase. Development of the local misorientation is due to increased dislocation content during plastic deformation according to Chakrabarty et al. [36]. The local misorientation value versus relative frequency is shown in Fig. 9. Local misorientation is associated with a misorientation less than 5° in this study. As seen in Fig. 9, the relative frequency of low local misorientation values (less than 0.5°) is highest in the undeformed specimens, while higher local misorientation values are more pronounced in the deformed specimens. In addition, with the increase in deformation, the peaks of the distribution of GBE and non-GBE specimens shift to the right gradually and the peak values of curves appear at 0.45° , 0.55° , 0.75° , 1.35° , which indicated higher misorientation angle with increasing strain. By comparing the relative frequency at each deformation, it can be seen that local misorientation peak values of GBE specimens are lower than those of non-GBE specimens. This indicates that the strain distribution in the GBE specimen is more uniform. On the other hand, interestingly, in Fig. 9 the peak value differences between GBE and non-GBE specimens with the same

Table 3 Average Schmid factor of the GBE and non-GBE specimens under different deformation conditions

Strain (%)	Average Schmid factor \bar{m}	
	GBE	non-GBE
0	0.453	0.445
5	0.444	0.437
10	0.437	0.431
20	0.427	0.421

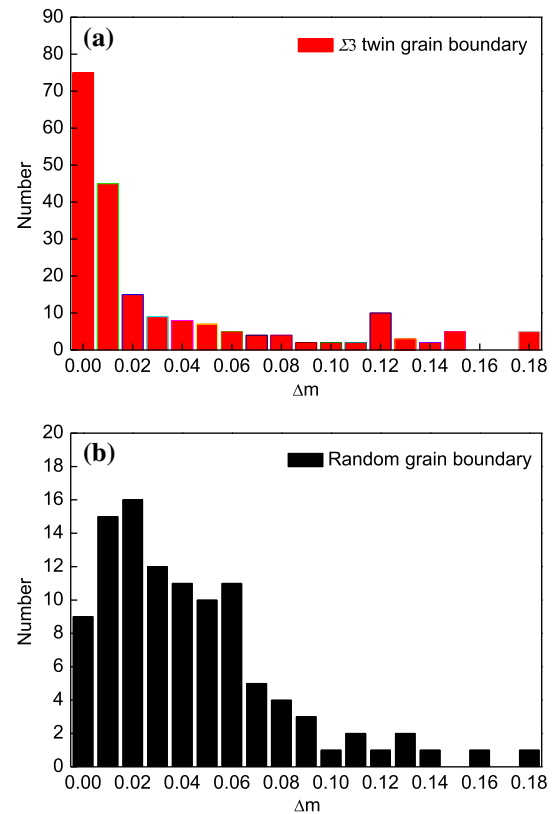


Figure 12 Distribution of the absolute values of Schmid factor mismatch (Δm) between the grains on both sides of **a** $\Sigma 3$ twin GBs and **b** random GBs.

deformation amount gradually decrease with increasing deformation, which indicates the local strain differences decrease. Sinha et al. [35] found that strain builds up from grain boundaries. At higher deformation, the strain spreads toward the interior of grains, which corresponds to the development of intragranular misorientation [35]. Therefore, the local strain differences between GBE and non-GBE specimens are significant at relative small deformation. In contrast, the strain spreads to grain interior as the material undergoes larger plastic deformation, leading to smaller local strain differences.

Figure 10 shows that the Vickers hardness tends to be lower for the GBE specimens than that for the non-GBE specimens in the cases of 5 and 10% tensile deformations. This is mainly because the GBE specimen has relatively high proportion of low- Σ CSL GBs resulting in a more homogeneous strain distribution. Lu et al. [37] found that the existence of large numbers of nanoscale twins may contribute to an increase

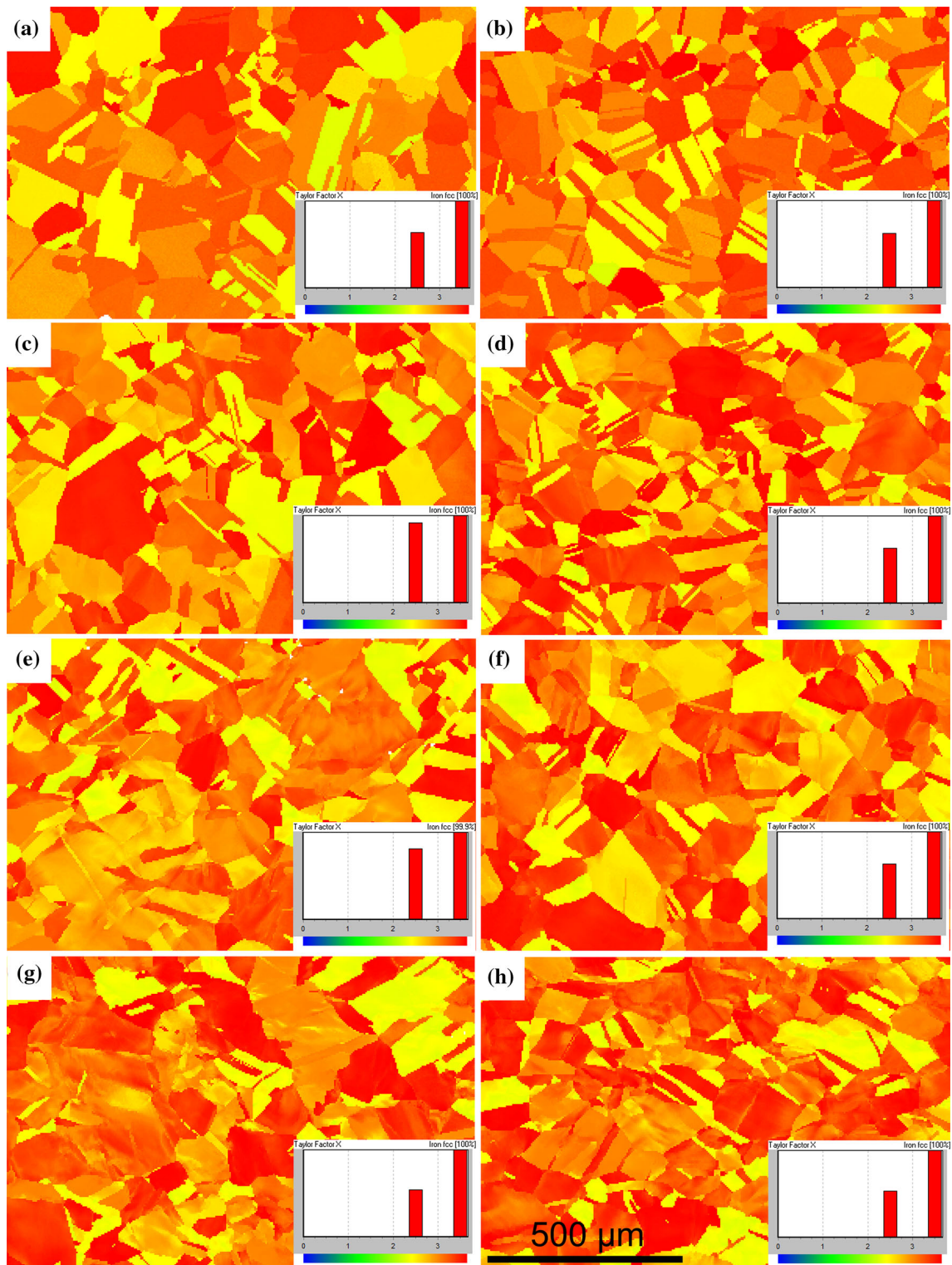


Figure 13 Taylor factor map of GBE and non-GBE specimens after different tensile deformations. **a** GBE-0, **b** non-GBE-0, **c** GBE-5%, **d** non-GBE-5%, **e** GBE-10%, **f** non-GBE-10%, **g** GBE-20%, **h** non-GBE-20%.

in the strength as well as to an improvement in the ductility of material. In nanocrystalline materials, nanoscale twin boundaries provide critical energy barriers, preventing slip transits from one twin to another, therefore leading to high strength. On the other hand, nanoscale twin boundaries have great capacity to accommodate dislocations, which favors to sustain ductility [37, 38]. However, in the GBE specimen with much larger grain size which are normally on the order of several tens micron, the $\Sigma 3$ twin boundaries have a weak interaction with dislocation, attributing to intrinsically high boundary cohesion associated with low energy [39]. In situ TEM straining also showed that screw dislocations can directly transmit through a coherent $\Sigma 3$ boundary when the slip planes on either side of the boundary are exactly aligned and the Burgers vector of the dislocation is fully preserved during the transmission [40]. Therefore, it can be deduced that pilling up of dislocations at random GBs is more pronounced than that at $\Sigma 3$ twin boundaries under the condition of small amount of deformation. Figure 10 also shows that the hardness values of both specimens are almost equivalent in the case of 20% tensile deformation. Almost all of the special structure boundaries lost the original “speciality” under the condition of 20% tensile deformation. In this case, a high density of dislocations is accumulated in both of the specimens leading to a similar hardness.

Schmid factor maps for GBE and non-GBE specimens after different tensile deformations are shown in Fig. 11. The Schmid factor (m) is calculated for the orientation at each point and the date displayed as a color in the map. As shown in Fig. 11, with the increase in deformation the areas of green (0.32–0.36) and blue (0.36–0.41) increase gradually, indicating that the values of m decrease in most of the grains.

The Schmid factor gives an indication of how easy it is for slip to occur for a particular slip system in single-crystal materials. Therefore, the concept of average Schmid factor (\bar{m}) is proposed, which can characterize the difficulty of slip for the plastic deformation of polycrystalline materials. In addition, Cui et al. [41] found that \bar{m} can measure the elongation to failure of Mg–Zn–Y alloy. The higher value of \bar{m} , the easier the slip, leads to the better plasticity. The formula of \bar{m} is as follows:

$$\bar{m} = \sum_i \frac{1}{2}(m_{\text{Min}} + m_{\text{Max}}) \cdot f_i = \frac{1}{2} \sum_i (m_{\text{Min}} + m_{\text{Max}}) \cdot f_i \quad (1)$$

where i stands for the number of intervals divided by the values of m ; m_{Min} and m_{Max} indicate the minimum and maximum values of m , respectively; f_i represents proportion of each interval; $\frac{1}{2}$ is the size of each interval which is calculated by using the average value of m_{Min} and m_{Max} . The calculated \bar{m} of GBE and non-GBE specimens after different deformations according to Fig. 11 and Eq. (1), are shown in Table 3. Comparison of the \bar{m} , Table 3, shows evidence that the values of \bar{m} in GBE specimens are higher than those of non-GBE specimens. Therefore, this observation would tend to suggest that the slip of GBE specimens is easier to carry out.

The absolute values of Schmid factor mismatch (Δm) between the grains on both sides of GBs are analyzed for a large number of GBs including 105 random GBs and 202 $\Sigma 3$ twin GBs. As shown in Fig. 12a, b, it can be seen that the distribution of the Δm for the $\Sigma 3$ twin GBs is obviously different from that of the random GBs. The Δm values for the $\Sigma 3$ twin GBs are mainly in the range of $0 < \Delta m < 0.02$, whereas random GBs have larger values of the Δm . Fukuya et al. [42] found that local high stress field occurred more frequently at the GBs where the difference in Schmid factor was larger between two adjacent grains. Therefore, it can be deduced that the grains on both sides of the random GBs have more obvious deformation incompatibility. Dislocation motion or deformation spread can be impeded when

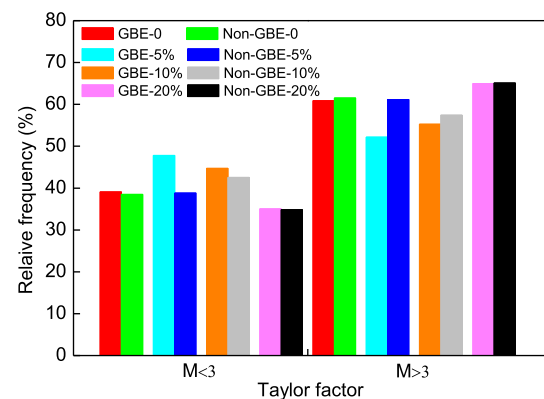
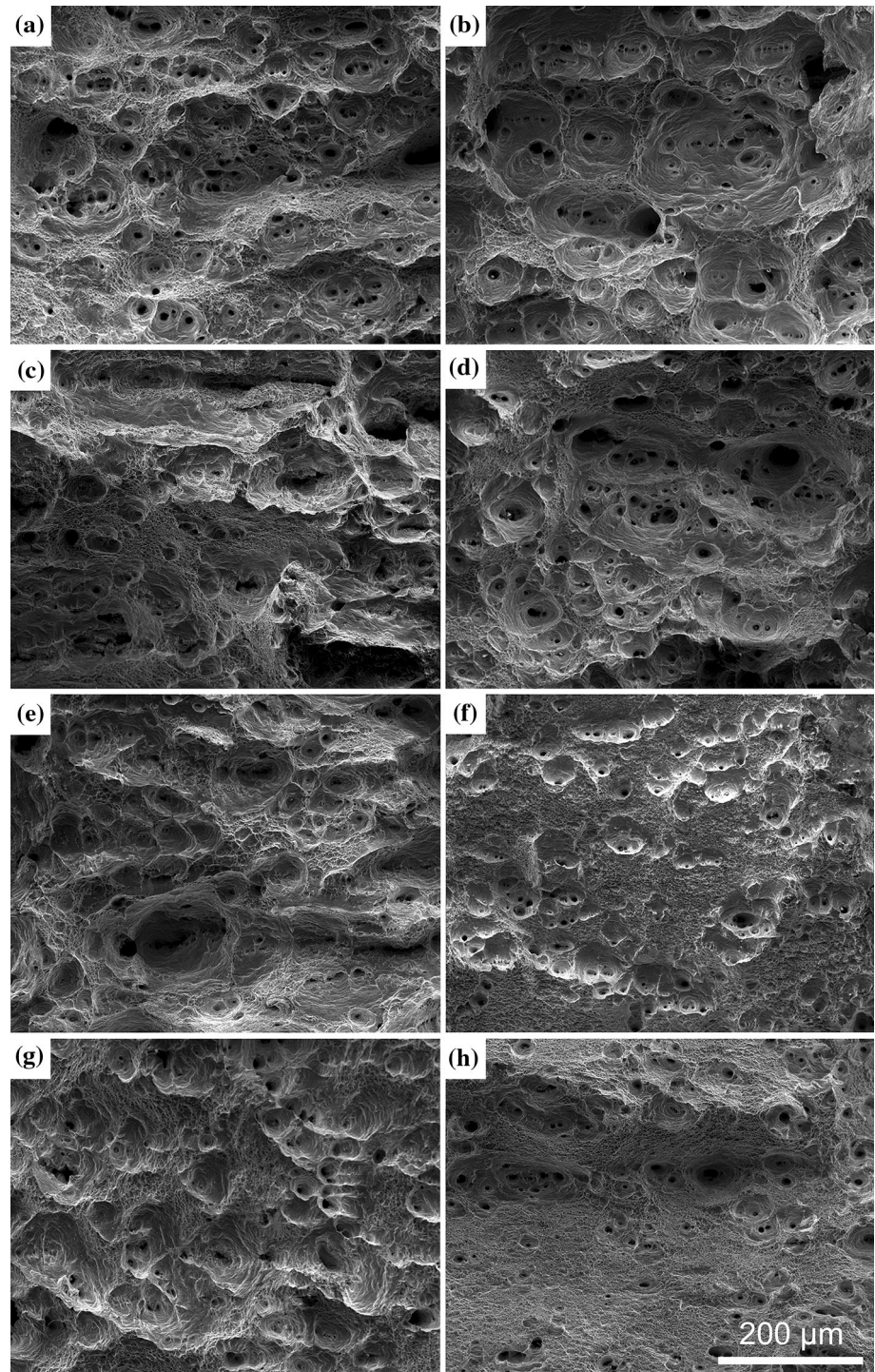


Figure 14 Distribution of Taylor factor for the GBE and non-GBE specimens under different deformation conditions.

Figure 15 Fracture surfaces of **a, c, e, g** GBE specimens and **b, d, f, h** non-GBE specimens at the strain rates of **a, b** $4 \times 10^{-2} \text{ s}^{-1}$, **c, d** $4 \times 10^{-3} \text{ s}^{-1}$, **e, f** $4 \times 10^{-4} \text{ s}^{-1}$, **g, h** $4 \times 10^{-5} \text{ s}^{-1}$.



random GBs are encountered, which leads to stress concentration. The transmission of dislocations across the $\Sigma 3$ twin boundaries is easier due to the better deformation compatibility between the adjacent twin grains. So the GBE specimen with high proportion of $\Sigma 3$ twin boundaries has a more homogenous strain

distribution and hence a higher uniform elongation and a lower hardness compared to the non-GBE specimen.

The Taylor factor (M) is also calculated in order to show the plastic deformation capacity of the GBE and non-GBE specimens as shown in Fig. 13. In

general, a higher value of Taylor factor indicates that macroscopic deformation requires larger slip shear strain and stress. Therefore, if a grain has a low Taylor factor, its deformation proceeds easier. Figure 13 shows that most of the grains of the GBE specimen have lower Taylor factor (yellow), while most of grains in the non-GBE specimen have higher Taylor factor values (red). Hence, the GBE specimen is initially softer. This can also be seen from the distribution of Taylor factors (Fig. 14): A higher relative frequency appears at low Taylor factor values ($M < 3$) for the GBE specimen, whereas the frequency of high value of Taylor factor ($M > 3$) is higher in the non-GBE specimen under all of the plastic deformation conditions.

Fractographs

Figure 15 shows the micro-appearances of the fibrous zones in the fractures of GBE and non-GBE specimens with different strain rates. The fracture surface morphologies indicate ductile fracture by the mechanisms of void nucleation. As shown in Fig. 15, the fractographs of the two specimens reveal dimpled rupture at all strain rates. The SEM micrographs in Fig. 15a–d show non-uniformly distributed dimples at the fibrous zones of the specimens which were tensile ruptured at relative high strain rates (4×10^{-2} and $4 \times 10^{-3} \text{ s}^{-1}$). In contrast, for the specimens ruptured at lower strain rates (4×10^{-4} and $4 \times 10^{-5} \text{ s}^{-1}$), the fractures have many smaller equiaxial dimples, as shown in Fig. 15e–h. The non-uniformly distributed dimples of the two specimens are due to the accelerated growth rate of micropores and cracks in the condition of high strain rate, resulting in higher fracture velocity. In addition, the dimples in GBE specimens are larger and deeper as compared to the non-GBE specimens. The phenomenon can be easily found in all conditions, especially at low strain rates. It has been reported [43] that the large and deep dimple structure corresponds to great plastic deformation ability and high fracture toughness. Therefore, the distribution of dimples also indicates improvement of plasticity by GBE processing.

Conclusions

The present investigation is aimed at applying GBE processing to 316L austenitic stainless steel and evaluating the associated mechanical properties. The

different thermomechanical processings (TMPs) were carried out to attain GBE and non-GBE specimens with a similar average grain size. The mechanical properties were evaluated by tensile tests at different strain rates, and the microstructures were characterized with SEM and EBSD to show the effects of GBCD on the deformation behaviors. Based on the results and observations presented in this study, the following conclusions can be reached:

1. Enhancing the proportion of low- Σ CSL GBs for GBE of 316LSS can be accomplished via 7% tensile deformation followed by annealing at 1050 °C for 30 min, and simultaneously the large size highly twinned grain cluster microstructure is formed.
2. The GBE specimens display increased uniform elongation during tensile tests at room temperature, and the differences in uniform elongations between the GBE and non-GBE specimens ($UE_{\text{GBE}} - UE_{\text{non-GBE}}$) increase with the decreasing of strain rate.
3. The GBE specimen with high proportion of $\Sigma 3$ twin boundaries has a more homogenous strain distribution during deformation as indicated by the local misorientation, Schmid factor and Taylor factor analysis.

Acknowledgements

This work was supported by the National Natural Science Foundation of China (NSFC) (Grant Number 51671122).

References

- [1] Ikeda S (2010) Technical progress of stainless steel and its future trend. Nippon Steel Tech Rep 99:2–8
- [2] Kumar BR, Chowdhury SG, Narasaiah N, Mahato B, Das SK (2007) Role of grain boundary character distribution on tensile properties of 304L stainless steel. Metall Mater Trans A 38(5):1136–1143
- [3] Sakaguchi N, Watanabe S, Takahashi H (2005) A new model for radiation-induced grain boundary segregation with grain boundary movement in concentrated alloy system. J Mater Sci 40(4):889–893. doi:10.1007/s10853-005-6506-3
- [4] Tsurekawa S, Okamoto K, Kawahara K, Watanabe T (2005) The control of grain boundary segregation and segregation-

- induced brittleness in iron by the application of a magnetic field. *J Mater Sci* 40(4):895–901. doi:[10.1007/s10853-005-6507-2](https://doi.org/10.1007/s10853-005-6507-2)
- [5] Raabe D, Herbig M, Sandlöbes S, Li Y, Tytko D (2014) Grain boundary segregation engineering in metallic alloys: a pathway to the design of interfaces. *Curr Opin Solid State Mater Sci* 18(4):253–261
- [6] Alexandreanu B, Was GS (2006) The role of stress in the efficacy of coincident site lattice boundaries in improving creep and stress corrosion cracking. *Scr Mater* 54(6):1047–1052
- [7] Boehlert CJ (2008) The effect of thermomechanical processing on the creep behavior of Alloy 690. *Mater Sci Eng A* 473(1–2):233–237
- [8] Hu CL, Xia S, Li H, Liu TG, Zhou BX, Chen WJ (2011) Improving the intergranular corrosion resistance of 304 stainless steel by grain boundary network control. *Corros Sci* 53(5):1880–1886
- [9] Palumbo G, Erb U (1999) Enhancing the operating life and performance of lead-acid batteries via grain-boundary engineering. *MRS Bull* 24(11):27–32
- [10] Michiuchi M, Kokawa H, Wang ZJ, Sato YS, Sakai K (2006) Twin-induced grain boundary engineering for 316 austenitic stainless steel. *Acta Mater* 54(19):5179–5184
- [11] Xia S, Li H, Liu TG, Zhou BX (2011) Applying grain boundary engineering to Alloy 690 tube for enhancing intergranular corrosion resistance. *J Nucl Mater* 416(3):303–310
- [12] Zhang ZW, Wang WH, Zou Y, Baker I, Chen D, Liang YF (2015) Control of grain boundary character distribution and its effects on the deformation of Fe–6.5 wt% Si. *J Alloys Compd* 639:40–44
- [13] Watanabe T (1984) Approach to grain boundary design for strong and ductile polycrystals. *Res Mech* 11:47–84
- [14] Kumar M, Schwartz AJ, King WE (2002) Microstructural evolution during grain boundary engineering of low to medium stacking fault energy fcc materials. *Acta Mater* 50(10):2599–2612
- [15] Watanabe T (2011) Grain boundary engineering: historical perspective and future prospects. *J Mater Sci* 46(12):4095–4115. doi:[10.1007/s10853-011-5393-z](https://doi.org/10.1007/s10853-011-5393-z)
- [16] Randle V, Coleman M (2009) A study of low-strain and medium-strain grain boundary engineering. *Acta Mater* 57(11):3410–3421
- [17] Li B, Tin S (2014) The role of deformation temperature and strain on grain boundary engineering of Inconel 600. *Mater Sci Eng A* 603(5):104–113
- [18] Randle V, Hu Y (2009) The role of vicinal $\Sigma 3$ boundaries and $\Sigma 9$ boundaries in grain boundary engineering. *J Mater Sci* 40(12):3243–3246. doi:[10.1007/s10853-005-2692-2](https://doi.org/10.1007/s10853-005-2692-2)
- [19] Liu TG, Xia S, Li H, Zhou BX, Bai Q (2014) Effect of the pre-existing carbides on the grain boundary network during grain boundary engineering in a nickel based alloy. *Mater Charact* 91:89–100
- [20] Engelberg DL, Newman RC, Marrow TJ (2008) Effect of thermomechanical process history on grain boundary control in an austenitic stainless steel. *Scr Mater* 59(5):554–557
- [21] Richard J, Randle V (2010) Sensitisation behaviour of grain boundary engineered austenitic stainless steel. *Mater Sci Eng A* 527(16–17):4275–4280
- [22] Lee SL, Richardsr NL (2005) The effect of single-step low strain and annealing of nickel on grain boundary character. *Mater Sci Eng A* 390(1–2):81–87
- [23] Rohrer GS, Randle V, Kim CS, Hu Y (2006) Changes in the five-parameter grain boundary character distribution in α -brass brought about by iterative thermomechanical processing. *Acta Mater* 54(17):4489–4502
- [24] Kobayashi S, Nakamura M, Tsurekawa S, Watanabe T (2011) Effect of grain boundary microstructure on fatigue crack propagation in austenitic stainless steel. *J Mater Sci* 46(12):4254–4260. doi:[10.1007/s10853-010-5238-1](https://doi.org/10.1007/s10853-010-5238-1)
- [25] Sinha S, Kim DI, Fleury E, Suwas S (2015) Effect of grain boundary engineering on the microstructure and mechanical properties of copper containing austenitic stainless steel. *Mater Sci Eng A* 626:175–185
- [26] Hansen N (2004) Hall–Petch relation and boundary strengthening. *Scr Mater* 51(8):801–806
- [27] Schino AD, Barteri M, Kenny JM (2003) Effects of grain size on the properties of a low nickel austenitic stainless steel. *J Mater Sci* 38(23):4725–4733. doi:[10.1023/A:1027470917858](https://doi.org/10.1023/A:1027470917858)
- [28] Wang ZG, Zhang ZF, Li XW, Jia WP, Li SX (2001) Orientation dependence of the cyclic deformation behavior and the role of grain boundaries in fatigue damage in copper crystals. *Mater Sci Eng A* 321(12):63–73
- [29] Detrois M, Rotella J, Goetz RL, Helmink RC, Tin S (2016) Grain boundary engineering of powder processed Ni-base superalloy RR1000: influence of the deformation parameters. *Mater Sci Eng A* 627:95–105
- [30] Palumbo G, Aust KT, Lehockey EM, Erb U, Lin P (1998) On a more restrictive geometric criterion for “special” CSL grain boundaries. *Scr Mater* 38(11):1685–1690
- [31] Lichtenfeld JA, Mataya MC, Tyne CJV (2006) Effect of strain rate on stress-strain behavior of alloy 309 and 304L austenitic stainless steel. *Metall Mater Trans A* 37(1):147–161
- [32] Campbell JD, Ferguson WG (1970) The temperature and strain-rate dependence of the shear strength of mild steel. *Philos Mag* 21(169):63–82

- [33] Liu YN, Zhu JH (1990) Strength of a low carbon steel at different temperatures and strain rates. *Chin J Mater Res* 4(4):285–290
- [34] Atwell DL, Barnett MR, Hutchinson WB (2012) The effect of initial grain size and temperature on the tensile properties of magnesium alloy AZ31 sheet. *Mater Sci Eng A* 549(7):1–6
- [35] Sinha S, Szpunar JA, Kumar NAPK, Gurao NP (2015) Tensile deformation of 316L austenitic stainless steel using in situ electron backscatter diffraction and crystal plasticity simulations. *Mater Sci Eng A* 637:48–55
- [36] Chakrabarty S, Mishra SK, Pant P (2014) Crystallographic orientation and boundary effects on misorientation development in austenitic stainless steel. *Mater Sci Eng A* 617:228–234
- [37] Lu K, Lu L, Suresh S (2009) Strengthening materials by engineering coherent internal boundaries at the nanoscale. *Science* 324(5925):349–352
- [38] Meyers MA, Mishra A, Benson DJ (2006) Mechanical properties of nanocrystalline materials. *Prog Mater Sci* 51(4):427–556
- [39] Lehockey EM, Palumbo G, Lin P (1998) Grain boundary structure effects on cold work embrittlement of microalloyed steels. *Scr Mater* 39(39):353–358
- [40] Lee TC, Robertson IM, Birnbaum HK (1990) TEM in situ deformation study of the interaction of lattice dislocations with grain boundaries in metals. *Philos Mag A* 62(1):131–153
- [41] Cui HW (2013) Plastically deformed and microstructural formation of icosahedral quasicrystalline reinforced Mg–Zn–Y alloys. PhD Dissertation, Shandong University
- [42] Fukuya K, Nishioka H, Fujii K (2011) An EBSD examination of SUS316 stainless steel irradiated to 73 dpa and deformed at 593 K. *J Nucl Mater* 417(1–3):958–962
- [43] Gärtner F, Stoltenhoff T, Voyer J (2006) Mechanical properties of cold-sprayed and thermally sprayed copper coatings. *Surf Coat Technol* 200(24):6770–6782